ENGINEERING

# Critical assessment of water enthalpy characterization through dark environment evaporation

**Andrew Caratenuto[1] and Yi Zheng[1,2]***



**Comparative evaporation rate testing in a dark environment, commonly used to characterize a reduced vaporization enthalpy in interfacial solar evaporators, requires the assumption of equal energy input between cases. However, this assumption is not generally valid, leading to misleading characterization results. Interfacial evaporators yield larger evaporation rates in dark conditions due to enlarged liquid-vapor surface areas, resulting in increased evaporative cooling and larger environmental temperature differentials. Theoretical and experimental evidence is provided, which shows that these temperature differences invalidate the equal energy input assumption. The results indicate that differences in evaporation rates correspond to energy input variations, without requiring enthalpy to be reduced below theoretical values. These findings offer alternative explanations for previous claims of reduced vaporization enthalpy and contradict enthalpy-related conclusions drawn from differential scanning calorimetry. We conclude that postulating a reduced vaporization enthalpy using the dark environment method is inaccurate and that re-evaluation of vaporization enthalpy reduction is required.**

## INTRODUCTION

With the global water crisis becoming increasingly pervasive, research into effective mitigation methods has become very popular in recent years. Within this field, a boom of publications has emerged in the subfield of interfacial solar evaporation, whereby solar irradiance can produce clean water with high efficiency via thermal evaporation (*1*). A great number of interfacial evaporation devices have been demonstrated for this purpose, designed to float on the surface of nonpurified brine water, absorb solar irradiance, and continuously evaporate the impure water (*2*). Once evaporated, the purified water can be condensed for use, typically within some variation of a solar still.

To enhance water yield, it is highly desirable to maximize the efficiency of the evaporation process, typically by reducing parasitic energy losses to the environment. For an interfacial evaporator under solar irradiance, the steady-state evaporative heat flux can be described by

$$q_{\text{evap}} = \dot{m} h_{fg} = \eta q_{\text{sol}} \tag{1}$$

where $\dot{m}$, $h_{fg}$, $\eta$, and $q_{\text{sol}}$ are the evaporation rate, water phase change enthalpy, evaporation efficiency, and incident solar power, respectively. The evaporation efficiency describes the amount of incident solar irradiance used for the evaporation process, which may be reduced below 100% by parasitic heat losses from convection, radiation, and conduction (*2*).

In an ideal case under 1 sun (1000 W $m^{-2}$) irradiance, the maximum theoretically achievable evaporation rate is approximately 1.5 kg $m^{-2}$ $hour^{-1}$. Despite this, many researchers have obtained evaporation rates far above this limit, even without fully isolating the evaporation system from parasitic heat losses (*1*, *3*–*10*).

The typical explanation for this phenomena, introduced by Yu and colleagues in 2018, is that the vaporization enthalpy of water within the interfacial evaporators is reduced, thereby reducing the energy required to vaporize a given mass of water and allowing evaporation rates in excess of the theoretical limit (*3*). The proposed mechanism for this enthalpy reduction involves a weakening of the hydrogen bond network of water (or "water activation"), resulting from interactions with the hydrophilic porous structure of the interfacial evaporator (usually a hydrogel). They further postulate that water, in this modified state, may evaporate more readily in the form of clusters, with some hydrogen bonds still intact (*3*, *4*). After this point, the clusters may break apart outside of the system (i.e., above the evaporator), reducing the energy requirement for the evaporator itself.

A variety of characterization methods were used to defend this hypothesis, many of which are frequently used in contemporary studies to justify evaporation rates above the theoretical limit and prove that the vaporization enthalpy of water has been reduced. One of the most commonly used methods involves evaluating evaporation rates in the absence of solar irradiance (i.e., in a dark environment). In the dark environment evaporation test, the mass loss of identical water-filled beakers—one of pure water, and one with the interfacial evaporator placed on top—is monitored over an extended duration. With the assumption that the energy input from the environment (which facilitates pseudosteady evaporation over the test period) is equal between the two beakers during the process, one can conclude that

$$\left(\dot{m} h_{fg}\right)_{\text{H}_2\text{O}} = \left(\dot{m} h_{fg}\right)_{\text{evap}} \tag{2}$$

Thus, if the evaporation rate of the interfacial evaporator is higher than that of pure water in these conditions, this method offers a simple indicator that the vaporization enthalpy of water within the evaporator must be reduced (*1*, *3*).

However, deeper investigation reveals that this method produces misleading results that should not be used to justify a reduced vaporization enthalpy, due to the invalidity of the equal energy input assumption. Here, we show both theoretically and experimentally that differences in the dark environment evaporation rate are primarily due to differences in interfacial surface area, which invalidates the assumption of equal energy input (Fig. 1). It is illustrated

[1]Department of Mechanical and Industrial Engineering, Northeastern University, Boston, MA 02115, USA. [2]Department of Chemical Engineering, Northeastern University, Boston, MA 02115, USA.
*Corresponding author. Email: y.zheng@northeastern.edu

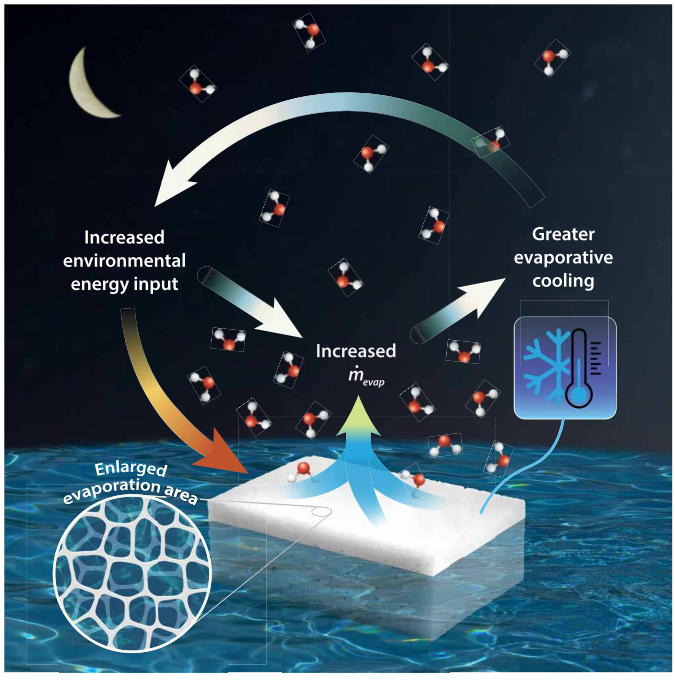


**Fig. 1. Mechanism of enhanced dark environment evaporation from an evaporator with enlarged interfacial surface area.** The enlarged interfacial surface area due to meniscus curvature within pores increases evaporation, inducing greater evaporative cooling, thus lowering the temperature of the evaporator and allowing it to harvest additional energy from the environment.

that energy input discrepancies due to differences in system temperatures are proportional to differences in evaporation rates. Modeling results show good agreement with the experiment, supporting these findings. Last, we provide data to show that differential scanning calorimetry (DSC) methods, which are commonly used to characterize vaporization enthalpy, are not in agreement with the results of the dark environment test.

## RESULTS

Left at rest in ambient conditions, water in a beaker will spontaneously evaporate as liquid molecules at the interface gain enough energy to overcome surface binding energy. In doing so, energy exits the water system through the latent heat of the exiting water vapor. This energy output manifests as a sensible heat reduction in the remaining liquid water, cooling the water. As the water temperature falls below the ambient temperature via evaporative cooling, the water will begin to receive energy from the environment due to the temperature differential, compensating for evaporative energy losses. Pseudosteady evaporation is achieved when the net energy input from the environment is equal to the energy output due to evaporation (*11*, *12*).

It is well known that natural evaporation rates are heavily dependent on the interfacial area, and that enlarging the evaporation surface will accelerate mass transfer. Many interfacial evaporators have substantially enlarged liquid-vapor surface areas, typically obtained via an internal porous structure, which intrinsically enhances the natural evaporation rate due to the curvature of menisci within pores (*13*, *14*). Furthermore, other factors such as pressure modification within a porous structure or the modification of surface energies have been reported to further enhance evaporation (*1*, *15*). All of these factors are generally desirable for increasing the evaporation rate, which can be clearly shown by an enhancement of evaporation under dark conditions.

However, these evaporation-enhancing factors have not been shown to inherently reduce the total energy requirement of evaporation. Under steady evaporation conditions, evaporative cooling must be balanced by energy from the environment via radiation, convection, and conduction. Energy input from any of these mechanisms is proportional to the temperature difference between the ambient environment and the surface(s) of the evaporation system. Therefore, for a fixed ambient temperature, an evaporation system with lower temperatures at steady state will receive a greater energy input from the environment.

In the context of a typical comparative dark environment test, the enhanced natural evaporation of the interfacial evaporator will induce greater cooling, which, in turn, induces a greater environmental energy input. This temperature difference may appear small—often less than 1°C between the water and evaporator systems—yet as will be shown, can cause appreciable discrepancies between the energy input of the two systems. As a result, the interfacial evaporation device receives substantially more energy input and can sustain enhanced evaporation rates in comparison to water without relying on the hypothesis of reduced vaporization enthalpy. In short, enhanced evaporation resulting from the properties of the interfacial evaporator produces a greater evaporative cooling effect, which enables greater environmental heat fluxes that can maintain larger evaporation rates (Fig. 1).

### Theoretical heat transfer model

To prove that the temperature differences that result from disparate evaporation rates are not negligible in a comparative dark environment evaporation test, theoretical calculations are performed. Consider a beaker of diameter $d$ and height $H$ filled with water, placed on a thick piece of insulating foam. In general, convective and radiative transfer between a surface of the beaker and the environment can be described by the following equations (*11*)

$$q_{\text{conv}} = A_i h_i \left(T_\infty - T_i\right) \tag{3}$$

$$q_{\text{rad}} = A_i \varepsilon_i \sigma \left(T_\infty^4 - T_i^4\right) \tag{4}$$

In these equations, the subscript $i$ is used to designate the appropriate surface of the beaker. $A$ is the area of the surface, $h$ is the convection coefficient, and $T_\infty$ is the ambient temperature, $T$ is the beaker surface temperature, $\varepsilon$ is the emissivity of the surface, and $\sigma$ is the Stefan-Boltzmann constant. The Nusselt number is used to calculate natural convection coefficient for the horizontal top surface and vertical walls of the beaker, respectively, as (*11*)

$$\begin{aligned} Nu_L &= 0.54 Ra_L^{1/4} \text{ for } Ra_L < 10^7 \\ Nu_L &= 0.15 Ra_L^{1/3} \text{ for } Ra_L \geq 10^7 \end{aligned} \tag{5}$$

and

$$Nu_L = \left\{ 0.825 + \frac{0.387 Ra_L^{\frac{1}{6}}}{\left[1 + \left(\frac{0.492}{Pr}\right)^{\frac{9}{16}}\right]^{\frac{8}{27}}} \right\}^2 \tag{6}$$

Air properties are evaluated at the average temperature between the ambient and the surface. The wall of the beaker is assumed to have negligible thermal resistance due to its low thickness.

The beaker is also assumed to be insulated on the side and/or bottom surfaces (depending on the case). For simplicity, steady state is assumed, such that changes in sensible heat can be neglected. The accuracy of these assumptions will be revisited in later sections with respect to the experimental results.

The diameter and height of the beaker are 41 and 40 mm, respectively, and the Stefan-Boltzmann constant is taken as $5.67 \times 10^{-8}$ W m$^{-2}$ K$^{-4}$. The emissivities of the water, beaker, and evaporator are taken as 0.96, 0.95, and 0.92, respectively. When the side walls of the beaker are considered, the wall temperature is set based on the prescribed ambient and surface temperatures. Surface-wall differentials range from about 0° to 1.5°C and are based on a fitting of several trials of steady-state experimental data using a system of comparable parameters. Further details on emissivity values and wall temperatures are given in the Supplementary Text.

Using these methods, the environmental energy input for a beaker undergoing steady evaporation is quantified. By modeling and comparing beakers with different surface temperatures in the same ambient conditions, the energy impact of these temperature differentials is quantified. In this way, an input energy enhancement factor, which describes the excess energy input brought on by lower system temperatures (as may result due to the enhanced evaporation of an interfacial evaporator), can be defined as $f_{in,evap} = U_{in,evap}/U_{in,H_2O}$, where $U_{in,evap}$ and $U_{in,H_2O}$ represent the net input energy from the environment to the interfacial evaporator and water system, respectively. Thus, the energy enhancement factor provides a reasonable estimate for the energy input differences between the water and evaporator systems during a comparative dark environment evaporation test.

## Analytical results

The results of these theoretical analyses are shown in Fig. 2. First, an ambient temperature of 20°C is studied, with water surface

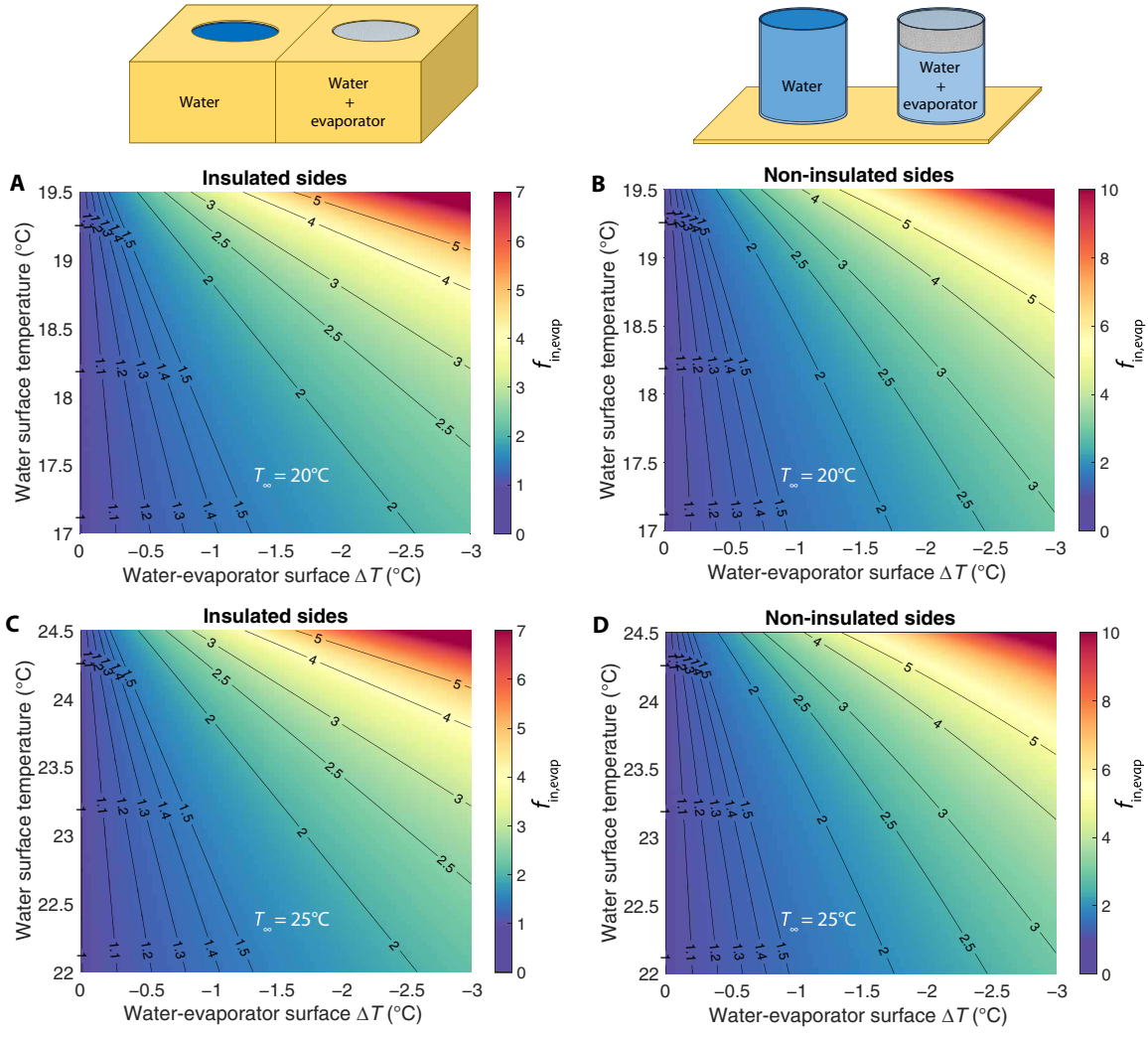


**Fig. 2. Theoretical modeling results.** Input energy enhancement factor $f_{in,evap}$ as a function of water and interfacial evaporator surface temperatures under a fixed ambient temperature $T_\infty$. (**A**) and (**B**) present results for cases of insulated and noninsulated side walls of the beakers, respectively, at $T_\infty$ = 20°C. (**C**) and (**D**) show the same two cases with an ambient temperature of $T_\infty$ = 25°C.

temperatures ranging from 17° to 19.5°C (*y* axis). The interfacial evaporator beaker is designated with a temperature difference from 0 to 3°C below that of the pure water (*x* axis). From Fig. 2A, it is immediately apparent that even small surface temperature differences can cause quite large differences in energy input. The energy input to the evaporator system can exceed 1.5 times that of the water system even with a temperature differential less than 1°C. At greater differentials, the evaporator system can easily obtain 2 to 3 times as much energy from the environment as the pure water system.

As expected, the energy input enhancement factor $f_{in,evap}$ is heavily dependent on the chosen temperature differential between the water and evaporator systems, as all heat transfer components are directly proportional to this quantity. In addition, if the chosen water temperature is closer to the ambient temperature, the relative energy gain from the corresponding evaporator case is larger. This is because the ratio of the evaporator-ambient temperature difference and the water-ambient temperature difference becomes quite large in these cases.

When the sides of the beaker are not insulated (i.e., convective and radiative heat transfer from the sides is considered), the trends are quite similar, as seen in Fig. 2B. In addition, the choice of ambient temperature has a minimal impact, which is expected (Fig. 2, C and D). The ambient temperature essentially only modifies the convection coefficients through the air properties, and in the range of temperatures modeled here, air does not experience property changes that mainly impact convection. Thus, the impact of ambient temperature is minimal in comparison to the temperature differentials, which emerge as the obvious driving factors. Together, these observations indicate that the conclusions are largely setup and environment independent, and thus transferable to comparative dark environment tests across different laboratory environments and for various common beaker setup choices (insulated or noninsulated).

The most important takeaway of the analytical results concerns the magnitude of the differences in energy input. The model indicates that temperature differences in the range of 0° to 3°C may provide the evaporator with far more energy than the water system, more than doubling its energy input in many cases. Thus, this enhanced energy input would explain evaporation rates of interfacial evaporators that exceed those of water by similar factors without necessitating claims of reduced vaporization enthalpy.

## Experimental validation

### *Evaporation tests*

To further support these claims, comparative dark environment tests are performed (Fig. 3). The interfacial evaporator chosen for these tests is a simple melamine foam (MF) sponge, exemplified previously as an interfacial solar evaporator (*7*). This evaporator demonstrates superb water transport, high hydrophilicity, and has an open-porous structure with an average pore diameter of approximately 30 μm, as seen from the scanning electron microscopy (SEM) images (Fig. 3B and fig. S1). Crucially, the pore sizes, low water contact angle (fig. S4), and extremely high porosity of the MF sponge [about 99% (*16*)] yield an enhanced interfacial evaporation area due to capillary effects. Following the estimation scheme of Bongarala



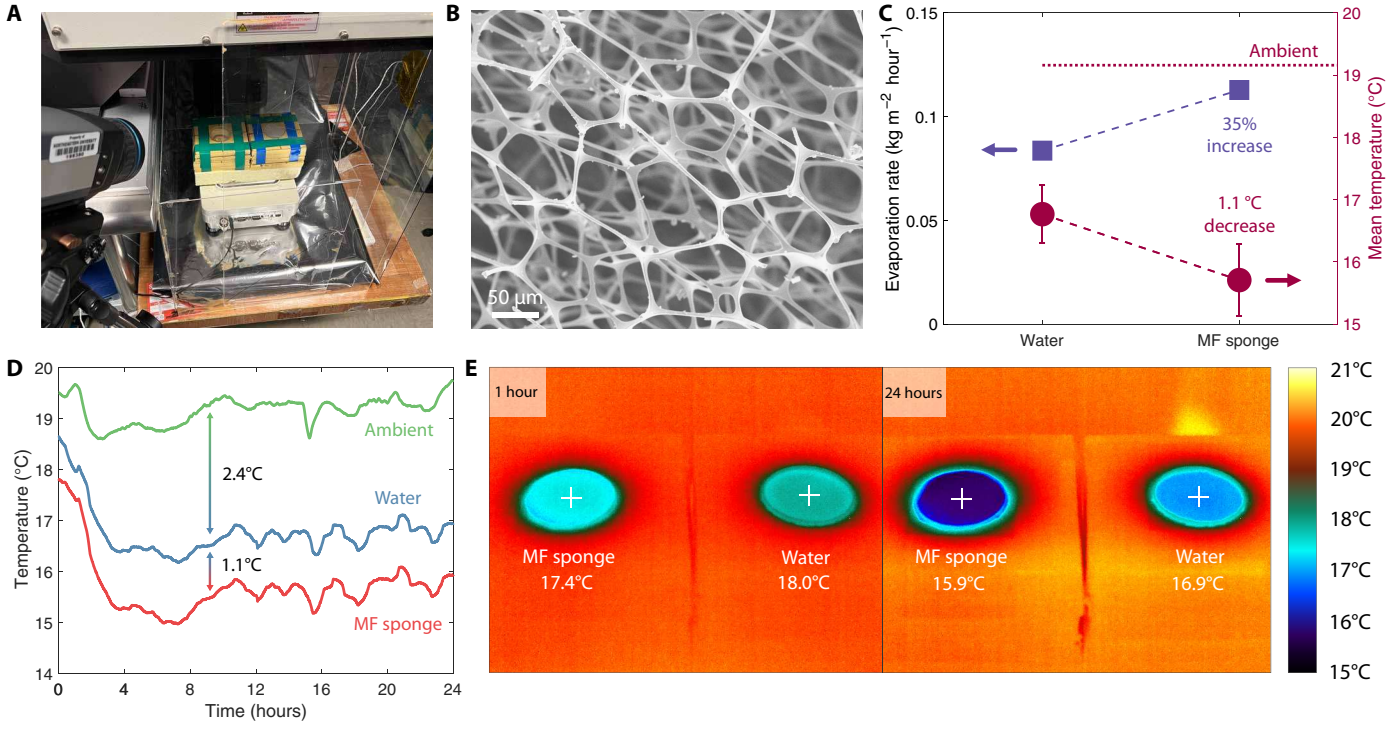


**Fig. 3. Experimental results for the comparative dark environment evaporation test.** (**A**) Dark environment system setup. (**B**) SEM image of the open porous structure of the MF sponge evaporator. (**C**) Twenty-four–hour dark environment evaporation rate and mean evaporation surface temperature for the water and MF sponge evaporation systems. Error bars indicate standard deviations of surface temperature over the 24-hour test period. (**D**) System temperatures during the evaporation test. (**E**) IR camera images of both systems during the test, showing their disparate evaporation surface temperatures.

*et al.* (*14*), the liquid-vapor surface area of a water-saturated MF sponge may nearly double as compared to a corresponding flat surface as a result of meniscus curvature within pores. In practice, this is likely an overestimate. The MF sponge's pores are irregular and not perfectly spherical, as seen from the SEM images, and the contact angle may fluctuate as water transport occurs throughout the structure, both of which may reduce this value. Thus, while the upper limit of evaporation area enhancement from the MF sponge based on porosity and contact angle is about 1.98, the actual enhancement is expected to be lower based on deviations from the idealized model (*14*).

For the comparative dark environment test, two beakers containing deionized (DI) water are placed side by side in blocks of insulation, as shown in Fig. 3A and fig. S5. The MF sponge is placed on the water surface of the evaporator beaker, in direct contact with the water, with its top surface in line with the mouth of the beaker. Temperatures of each evaporation system and the environment are monitored using an infrared (IR) camera and confirmed with thermocouples, and the mass of each beaker is weighed before and after 24 hours to determine the mass loss by evaporation. Further details are provided in Materials and Methods.

The experimental results confirm our key hypothesis: the interfacial evaporator system maintains notably lower temperatures than the water system throughout the entirety of the test. While both systems display a fairly consistent temperature differential with the ambient after an initial transient period of about 6 hours, the MF sponge maintains a temperature nearly 1.1°C below that of the water surface under identical ambient conditions, as shown in Fig. 3 (C and D).

As expected, the use of the interfacial evaporator yields an enhanced evaporation rate, as shown in Fig. 3C. The water beaker achieves an evaporation rate of 0.084 kg $m^{-2}$ $hour^{-1}$ during the 24-hour test. In contrast, the MF sponge achieves a 35% higher evaporation rate over the same period (0.113 kg $m^{-2}$ $hour^{-1}$). The porous structure of the MF sponge enhances the evaporation rate primarily due to its enlarged evaporation area; its pore sizes are in the double-digit micrometer range, which is not expected to cause any appreciable difference in internal pressure (*7*, *17*). However, this characteristic has no effect on the energy required for water to evaporate from its porous structure. Instead, its ability to maintain higher evaporation rates is due to its lower interfacial temperatures (clearly seen in the IR camera images of Fig. 3E), which allow for a greater energy input from the environment.

### *Transient model*

To support these conclusions, transient analyses are performed on the experimental temperature data. The energy balance for the entire beaker during the test can be expressed as

$$q_{evap} = \dot{m}h_{fg} = q_{conv} + q_{rad} + q_{cond} + q_{sens} \quad (7)$$

where $q_{cond}$ and $q_{sens}$ represent conductive and sensible heat contributions. This equation is consistent with earlier theoretical descriptions of the evaporation process, where energy loss from evaporation is balanced by cooling of the water itself and environmental energy inputs. This relationship enables quantification of the energy transfer components and estimation of the vaporization enthalpy of each beaker, which will further illustrate that the assumption of equal energy input is invalid, and that there is no reduction in vaporization enthalpy.

A transient, axisymmetric heat transfer model is run for each beaker using the Matlab PDE toolbox (*18*). The boundary condition at the top surface for each time step is set as the experimentally measured surface temperature of the evaporation surface. The side and bottom walls are designated with conductive heat flux boundary conditions, based on measured values of the insulation thickness and thermal conductivity, and water properties are approximated as constant due to the low range of temperatures. Further information regarding model input parameters is provided in the Supplementary Text.

On the basis of these inputs, the temperature distribution inside the beaker is calculated at each time step over the 24-hour test period. The solution is nonlinear, as conductive and sensible heat inputs are determined based on the resulting temperature field. Transient convective and radiative inputs at the evaporation surface are determined using Eqs. 3 to 5. The ambient air temperature is used for the convection calculation, while the enclosure wall temperature is used for the radiative calculation. Thus, all contributing energy input components are determined for the experimental test.

The results of these analyses are provided in Fig. 4. From Fig. 4 (A, C, and D), the bottom and mean surface temperatures of each beaker are higher than the evaporation surface, as expected. The maximum temperature is maintained at the bottom of each beaker, as it is farthest from the cold evaporation surface while still receiving energy input from the surroundings. Model mean and bottom temperatures respond accordingly to changes in ambient and surface temperatures, yet are temporally delayed due to the large specific heat of water. At all times, the entire MF sponge beaker maintains bulk and interface temperatures below that of the water beaker.

The cumulative energy input from each heat transfer mechanism is shown in Fig. 4B. For all mechanisms, the MF sponge beaker receives more energy than the water beaker. The lower temperatures of the MF sponge system induce greater heat transfer through an increased temperature differential with the environment, resulting in approximately 40% more energy input for most heat transfer mechanisms. For convection, this percent increase is even larger, nearing 60%. Convection input to the MF sponge system is enhanced not only by an increased environmental temperature differential, but also by a slight increase in the convection coefficient (fig. S4). Even the sensible heat contribution, though small, is enhanced by the lower system temperatures of the MF beaker. Conduction from the side walls emerges as a key contributor to the energy input of both systems. However, it is important to note that the side wall area is nearly four times as large as the top or bottom surfaces, over which the other environmental inputs act upon. Thus, on the basis of heat flux, convection and radiation on the top evaporation surface are the largest contributors. This outcome is expected, as the largest environmental temperature differential exists at this location.

By combining these results with Eq. 7, the vaporization enthalpy of each beaker can be calculated, shown in Fig. 4E. Analysis of the water beaker yields an enthalpy value of 2370 J $g^{-1}$, while that of the MF sponge beaker is 2558 J $g^{-1}$. The values of both beakers agree with the theoretical value of 2460 J $g^{-1}$ (*19*) within less than 4%. This result clearly illustrates that the vaporization enthalpy of water within the MF sponge is not reduced, but that the assumption of equal energy input used in the comparative dark environment test is invalid. The MF sponge receives a greater energy input based on its

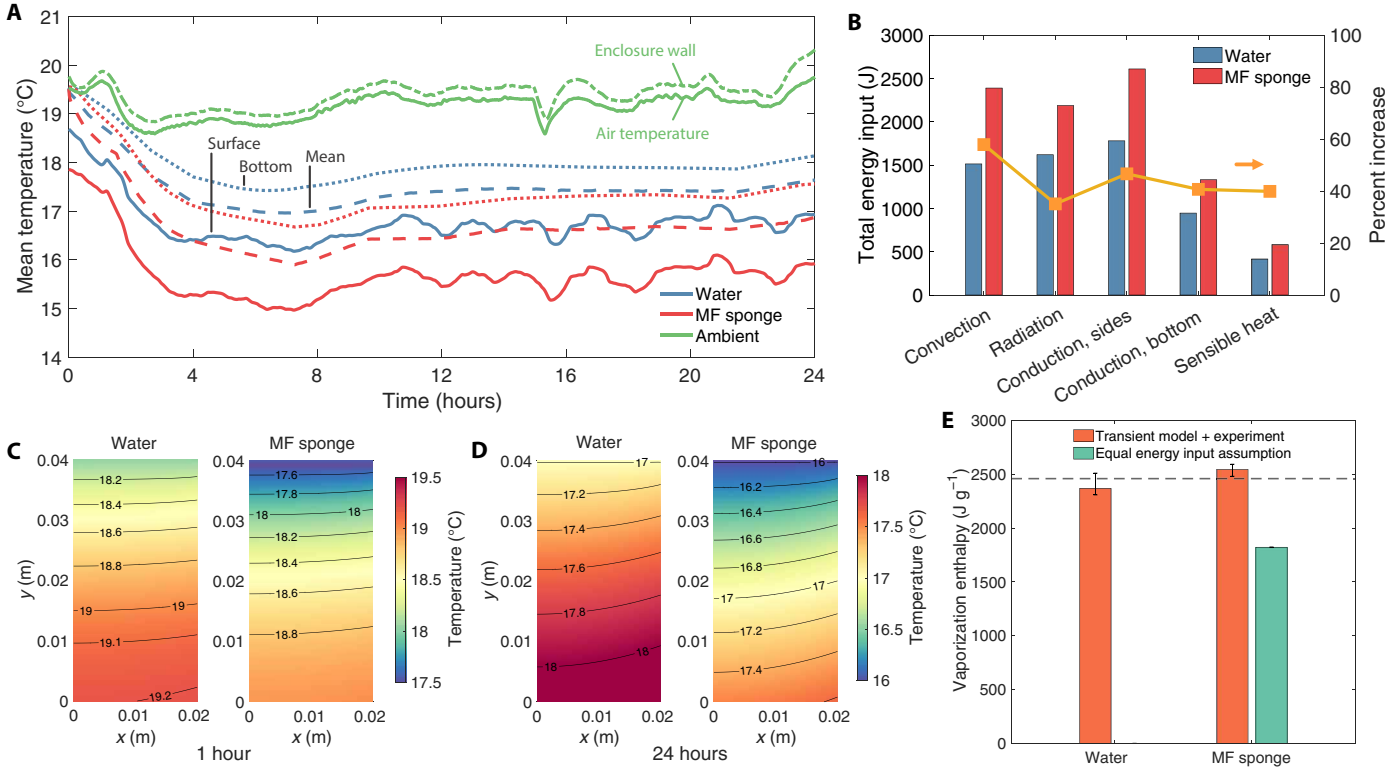


**Fig. 4. Experimental analysis using transient model.** (**A**) Temporal data for experimental system and resulting system temperatures based on transient model. Solid, dashed, and dotted lines for beaker systems represent the surface (experimental), bulk mean (model), and bottom (model) temperatures, respectively. (**B**) Cumulative energy input from different environmental heat transfer mechanisms over the 24-hour test period. Yellow markers denote percent increase in each component when the MF sponge is used, corresponding to the right axis. Modeled axisymmetric temperature profiles within the beakers at (**C**) 1 hour and (**D**) 24 hours. (**E**) Calculated vaporization enthalpy determined from the transient model analysis. The dotted line indicates the theoretical enthalpy value of 2460 J $g^{-1}$. Error bars indicate model results based on an IR camera measurement uncertainty of ±0.05°C. The secondary green bar shows the erroneous enthalpy value for the MF sponge that would be obtained if the equal energy input assumption were used.

lower temperatures, which corresponds with great accuracy to its enhanced evaporation rate. If the equal energy input assumption were used for this test, a vaporization enthalpy value of 1823 J $g^{-1}$ would have been established. Thus, it is easy to see how misleading results of vaporization enthalpy reduction are obtained using this method. These experiments and analyses show clearly that, when energy inputs from the environment are properly accounted for, there is no indication of vaporization enthalpy reduction. Further support for the reliability of these analyses is provided in the Supplementary Text and fig. S8.

### *Hydrogel evaporators*

Porous interfacial evaporators for solar evaporation can generally be separated into two categories: those that modify the bonding state of water within their porous structure due to the presence of bound water, and those that do not. The MF sponge is a good representation of the latter category. The preceding results and analyses clearly show that, for these types of evaporators, enhanced evaporation in a dark environment can be attributed entirely to interfacial surface area effects as opposed to claims of reduced vaporization enthalpy. To generalize these conclusions to all types of evaporators, comparative evaporation tests and analyses are extended to hydrogel evaporators.

Hydrogels are used commonly for solar evaporation applications, largely due to claims that their influence on water bonding within their porous structures effectively reduces water vaporization enthalpy by weakening the hydrogen bonding network (*1*). To assess this claim, comparative dark environment tests are repeated for polyvinyl alcohol (PVA) hydrogels fabricated based on representative works in the literature (*3*, *20*, *21*). Three hydrogel samples are synthesized (fig. S9) and evaluated the dark environment evaporation tests. The name of each sample is indicated with the PVA precursor solution ratio [7.5 or 10 weight % (wt %)]. When used, freeze-thaw cycles (one or five cycles) are also specified. More information on hydrogel sample synthesis is provided in Materials and Methods.

First, SEM images of all hydrogel samples are presented in Fig. 5 and figs. S10 to S12. PVA-7.5 and PVA-10-FTx5 show open porous structures with fairly high porosities; however, their porosities appear lower than that of the MF sponge. The PVA-10-FTx1 sample shows pores of similar scale, but appears to have a less open structure than the other two hydrogels. While all hydrogels show some amount of inconsistency in porosity over larger areas (figs. S10 to S12), PVA-7.5 and PVA-10-FTx5 maintain a greater proportion of porous structure coverage as compared to PVA-10-FTx1. Although the latter sample shows many similar morphological characteristics, it also has large areas without pores and regions with semi-closed pores. Morphological differences between these hydrogels are attributed to the degree and type of cross-linking present within each

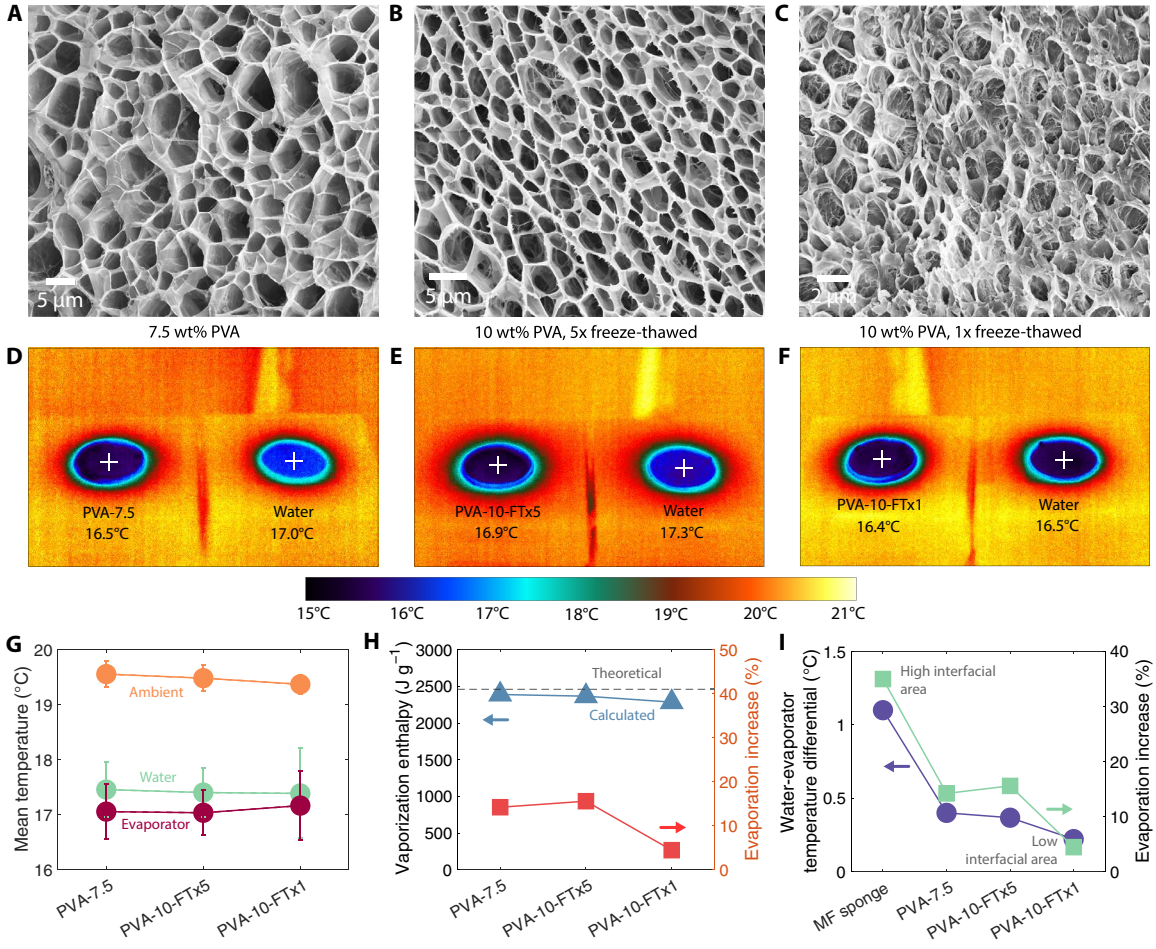


**Fig. 5. Hydrogel evaporator evaluation.** (**A** to **C**) SEM images of evaporator porous structures. Note that the porous structures of PVA-7.5 and PVA-10-FTx5 are more open than PVA-10-FTx1. (**D** to **F**) IR camera images of water and hydrogel evaporator beakers during the comparative test at 24 hours. (**G**) Mean ambient and surface temperatures during the evaporation test. Error bars indicate standard deviations of surface temperature over the 24-hour test period. (**H**) Vaporization enthalpy and evaporation increase with respect to water for each evaporator. Enthalpy is calculated based on heat transfer components during the comparative evaporation test. The dotted line indicates the theoretical value for water (evaluated at 17.5°C). (**I**) Mean water-evaporator surface temperature differentials during the evaporation test and corresponding percentage increases in evaporation with respect to water.

sample. Additional freeze-thaw cycles have been cited to increase pore size and crystallinity, due to the higher degree of phase separation induced by repeated cycling (*22*). This explains the more open and more ordered structure observed in PVA-10-FTx5 as compared to PVA-10-FTx1. Similarly, the lower PVA concentration used in PVA-7.5 also supports a more open porous structure with larger pores (*3*). Quantitative measures of porosity in these hydrogels are not made as structural variation between different regions is large, hindering accuracy when assessed by SEM. However, it can be generalized that PVA-7.5 and PVA-10-FTx5 samples have a greater interfacial evaporation area than PVA-10-FTx1, and a lower interfacial evaporation area than the MF sponge.

All three PVA hydrogels exhibit dark environment evaporation rates above that of water, along with surface temperatures below those of water (Fig. 5 and figs. S13 to S15). This is consistent with the theoretical description, as well as the results obtained for the MF sponge. Notably, the evaporation rate increase factors of the PVA-7.5 and PVA-10-FTx5 hydrogels (about 15%) are lower than that of the MF sponge (35%). Furthermore, the PVA-10-FTx1 evaporation rate is only 4% greater than that of water. These results agree with the porosity observations discussed previously and directly support the trend between interfacial surface area expansion and evaporation rate enhancement.

Further support is obtained from hydrogel temperatures during evaporation tests. The mean water-evaporator surface temperature differences for hydrogels (0.2° to 0.5°C) are lower in magnitude than that of the MF sponge (1.1°C). As mentioned previously, the excess energy received by the evaporator with respect to water is proportional to this temperature difference and is the driving factor in the enhancement of dark environment evaporation rates. This is clearly exemplified by comparing water-evaporator temperature differentials with evaporation rate increases. As shown in Fig. 5I, higher temperature differentials support greater evaporation rate increases due to enhanced energy input from the environment and align with the surface area enhancement deduced from SEM images. Thus, the relationship between liquid-vapor interfacial area, evaporation rate, and temperature is clearly shown to be consistent with the theoretical hypothesis. Last, for all three hydrogels, the

vaporization enthalpy determined from the experimental data and transient thermal model agrees well with the theoretical vaporization enthalpy of water. This indicates that even for hydrogel materials, dark environment evaporation rate increases are not due to vaporization enthalpy reductions, but rather due to input energy discrepancies stemming from variations in interfacial surface area.

***DSC characterization***

Last, evaporator samples are characterized using DSC to further support these conclusions. DSC data are commonly used to characterize transition enthalpies, and features of the heat flow curves can be analyzed for further information. DSC scans at high and low temperatures are frequently used for interfacial evaporators to prove their modified water state and/or reduced vaporization enthalpy, either on their own, or in conjunction with dark environment test data (*1*, *3*, *4*, *9*).

As shown in Fig. 6A, the DSC scan of pure water over the boiling point yields a vaporization enthalpy value close to the theoretical value, and shows a steep characteristic decline after all water is vaporized. The high-temperature DSC scans for the MF sponge show very similar results to those of water. Both profiles yield vaporization enthalpy values very close to the theoretical value of water. The vaporization enthalpy of water in the MF sponge decreases by only about 4% in comparison to pure water, and the two profiles share a very similar profile. In contrast, interfacial evaporators with modifications in water state will show DSC enthalpy values well below that of pure water, often showing reductions of 20% or more (vaporization enthalpy values below 2000 J $g^{-1}$). A broader, less steep profile is usually seen as well, and heat flow activity may persist past 100°C, both of which are attributed to the modified water bonding behaviors within the evaporators and/or the internal pressure reduction within hydrogels (*1*, *3*, *4*, *21*, *23*). None of these characteristics are visible for the MF sponge; hence, high-temperature DSC scans do not indicate any reduction in the vaporization enthalpy of water within the MF sponge. If the assumption of equal energy input were used in the MF sponge dark environment test, the results of the dark environment test would therefore be at odds with those of the DSC.

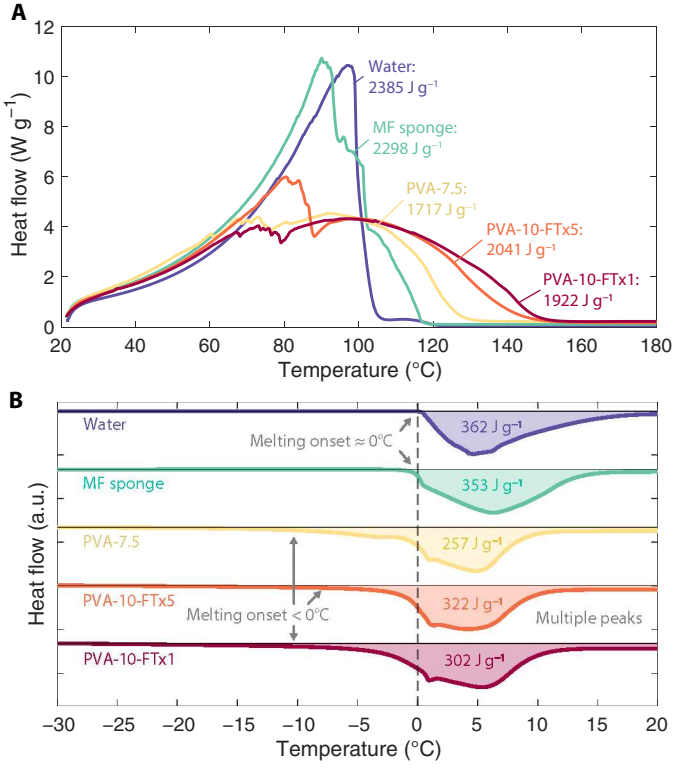


**Fig. 6. DSC characterization.** Heat flow curves for water and evaporator samples at (**A**) high temperatures and (**B**) low temperatures. Transition enthalpies, obtained through integration, are provided in the plots. A scanning rate of 10°C $min^{-1}$ is used for high-temperature characterization, while a rate of 5°C $min^{-1}$ is used for the low-temperature characterization.

On the other hand, all three hydrogel samples characterized in this work show nearly all of the aforementioned traits. DSC scans of the hydrogels yield enthalpy values from 2041 to 1717 J $g^{-1}$, representing respective reductions of 14 to 28% below the DSC-measured enthalpy value of water. The hydrogels also show broad profiles with heat flow activity, which persists far beyond 100°C. Thus, all three hydrogels show the typically cited characteristics of evaporators with reduced vaporization enthalpies. In contrast to this, the dark environment evaporation tests illustrate that the evaporation enhancement is purely due to energy input discrepancies, rather than vaporization enthalpy reduction. Therefore, the results of the DSC enthalpy characterization clearly contradict those of the dark environment evaporation tests when input energy differences are properly accounted for.

The DSC can also be used at low temperatures to gain information about the bonding state of water. Typically, for a modified water state as is commonly seen in hydrogels, the melting onset will shift well below 0°C, and the melting enthalpy often decreases. This impact stems from an increase in the bound water content of the hydrogel with respect to free water. While bound water itself is nonfreezable, intermediate water (also known as freezable bound water) will exhibit a lower freezing point than that of free water (0°C) (*1*, *4*, *24*, *25*). Both the water and MF sponge show a melting onset very close to 0°C (Fig. 6B). Both melting enthalpies are close to the theoretical value [334 J $g^{-1}$ (*25*)], and agree with one another within less than 3%. In contrast, all three hydrogel evaporators exhibit melting onsets well below 0°C, signifying notable intermediate water content. This is corroborated by the existence of multiple distinct melting peaks in the hydrogels, which are due to different states of water melting within the hydrogel, as well as lowered melting enthalpy values as compared to bulk water and water in the MF sponge (*1*, *4*, *24*, *25*). Hence, water in all three hydrogel samples show obvious signatures of a modified water bonding state, in direct contrast with the water and MF sponge. We note that the slight shift between the DSC profiles of PVA-10-FTx5 and PVA-10-FTx1 results from the more open structure of PVA-10-FTx5, in which a lower proportion of bound and intermediate water result from a higher water content (*24*).

Together, these low- and high-temperature DSC results clearly show that neither the vaporization enthalpy nor the hydrogen bonding state of water within the MF sponge is modified with respect to those of bulk water. Despite this, the dark environment test on its own would indicate a reduced vaporization enthalpy in the MF sponge if the assumption of equal energy input were used. The conclusions of the dark environment method (if the equal input energy assumption were used) and the DSC method of enthalpy characterization are therefore at odds with one another.

Further evidence is obtained by considering hydrogel evaporators. As characterized by DSC, all hydrogel evaporators explored here exhibit notable vaporization enthalpy reduction and water state modification, as well as evaporation enhancement in the dark environment. Yet, when properly accounting for input energy discrepancies during the dark environment evaporation tests, the calculated vaporization enthalpy agrees well with the theoretical value of water, in contrast with DSC results. In addition, the dark environment temperature differentials and evaporation increases observed for the PVA-7.5 and PVA-10-FTx5 samples are quite similar. This is expected, as they have similar evaporation surface areas (due to having similar porosities), providing similar dark environment results. Despite this, their DSC-measured vaporization enthalpy values are quantitatively dissimilar. This follows from their diversity from one another in several defining hydrogel traits, such as polymer mass content, cross-linking characteristics, and pore size, which have been cited to influence DSC-measured enthalpies of hydrogels (*1*, *3*, *4*, *23*, *26*). This case further exemplifies the contradictory nature of the dark environment and DSC enthalpy methods.

It is worth noting that discrepancies between reduced enthalpy values characterized via dark environment or DSC methods are commonly reported and are usually attributed to differences in the degree of dehydration experienced by the evaporator within each test (*3*). However, our data indicate that this explanation is insufficient. As shown from MF sponge and hydrogel evaporation tests, both types of evaporators exhibit enhanced evaporation in dark environments due to their expanded interfacial surface areas. This characteristic is independent of water state modification or enthalpy reduction attributes identified via DSC. Thus, we posit that DSC and dark environment enthalpy characterization methods show large discrepancies [often 500 J $g^{-1}$ or greater (*3*, *4*, *15*, *20*, *26*)] because they do not characterize the same phenomena regarding vaporization enthalpy, thus producing contradictory results for both types of evaporators. This aligns with the justification that DSC vaporization enthalpy reduction is instead due to pressure effects within hydrogels, as well as the demonstration of hydrogels without notable DSC-measured enthalpy reductions, which still exhibit evaporation rates in excess of the theoretical limit (*21*).

## DISCUSSION

The data and analyses reported herein clearly illustrate that comparative dark environment evaporation tests are not suitable for characterizing the reduced vaporization enthalpy of an interfacial evaporator. Enlarged evaporation surface areas or other evaporator characteristics may increase the evaporation rate in a dark environment, but this does not inherently modify the energy requirement of evaporation. Rather, increased evaporative cooling allows the evaporator system to reach a lower steady-state temperature, enabling it to harvest more environmental energy due to a greater temperature differential. Crucially, theoretical and experimental results show that the magnitude of this enhanced energy input is proportional to the enhanced evaporation observed in a dark environment. Furthermore, DSC results, which are commonly used to corroborate claims of reduced vaporization enthalpy in interfacial evaporators, are inconsistent with the dark environment results presented. Thus, it is concluded that comparative dark environment tests are not a valid method for establishing or quantifying a reduced vaporization enthalpy in an interfacial evaporator system, as the key assumption of equal energy input is not accurate. With this renewed context, the disparity of enthalpies determined by dark environment and DSC characterizations indicate that current justifications for reduced vaporization enthalpy in solar-driven evaporation systems require reconsideration.

To thoroughly and accurately demonstrate this concept, well-controlled experiments and detailed analytical models have been used. However, the utility of simple theoretical calculations in demonstrating this phenomenon is also apparent. If Fig. 2 were used to analyze the experimental data given in Fig. 3, an input energy increase of about 45% would have been noted, corresponding to an MF sponge evaporation rate about 45% larger than that of water. This is an overestimate, largely due to sensible heat and conductive contributions that are not accounted for. However, as most energy input mechanisms increase by roughly the same magnitude when the MF sponge is used, this simple method does offer a relatively close approximation, useful for benchmarking other reports in the literature.

Previous accounts of reduced enthalpy characterized using dark environment evaporation tests are widespread in the literature. Table 1 shows literature reports of reduced enthalpy obtained via the

**Table 1. Literature reports of reduced vaporization enthalpy (and associated ratio of evaporation increase) characterized using the dark environment evaporation method.**

| Material | $h_{fg,evap}$(J $g^{-1}$) | $f_{\dot{m}_{evap}}$ |
|---|---|---|
| Carbon cloth (*15*) | 2069 | 1.19 |
| PPy/Carbon cloth (*15*) | 1715 | 1.43 |
| Titanium suboxide powder (*9*) | – | 2.33 |
| PVA-PPy hydrogel (*3*) | 1377 | 1.75 |
| PVA-chitosan hydrogel (*4*) | 1030 | 2.38 |
| Adobe brick (*5*) | 1153 | 2.06 |
| Carbonized manure (*8*) | 1276 | 2.02 |
| MF sponge + Black 3.0 (*7*) | 1377 | 1.75 |
| Carbonized wood (*6*) | 2069 | 1.19 |
| Carbon foam (*26*) | 2013 | 1.22 |
| Lignocellulose aerogel (*10*) | 1434 | 1.71 |

dark environment evaporation method ($h_{fg,\mathrm{evap}}$). These values range from approximately 1000 to 2000 J $g^{-1}$. On the basis of Eq. 2, the enhancement factor of evaporation from the interfacial evaporator can be defined as $f_{\dot{m}_{\mathrm{evap}}} = h_{fg,\mathrm{evap}} / h_{fg,\mathrm{H_2O}}$. The reported values of $h_{fg,\mathrm{evap}}$ correspond to $f_{\dot{m}_{\mathrm{evap}}}$ values in the 1 to 2.5 range.

Looking back at the model results of Fig. 2, these accounts of reduced enthalpy could easily be explained by small variations in interfacial temperature during the dark environment tests as opposed to differences in vaporization enthalpy. It is difficult to assess past reports in the context of our model, as experimental temperatures during dark environment tests are scarcely reported. However, recent works show that water-evaporator surface temperature differences up to nearly 3°C are certainly reasonable (*9*). In addition, many of these comparative tests are not performed concurrently, meaning that the water and evaporator systems may experience differences in ambient temperature and humidity. This can lead to even further discrepancies in the environmental energy input, especially due to the influence of humidity, as described in the Supplementary Text. Considering these factors, the vaporization enthalpy reductions that are typically reported using the dark environment evaporation rate test correspond well with the magnitude of model-predicted excess energy input for a reasonable range of temperature differentials. Although some references report higher ratios of evaporation increase than our experimental results, we attribute this mainly to the fact that our tests, being performed concurrently, maintain better control of ambient conditions than many literature reports, which may perform evaporation tests at separate times and in separate conditions. Considering these factors, differences in environmental energy input provide a far more likely explanation for the disparate evaporation rates observed in comparative dark environment tests throughout the literature, as opposed to a reduction in vaporization enthalpy.

With the context of these experimental results, it is important to comment on the controversial role of the dark environment evaporation rate in the analysis of a solar-driven evaporation system (*12*, *27*). Often, the dark environment evaporation rate is subtracted from the evaporation rate under solar irradiance to obtain a dark-excluded evaporation rate. The goal of this is to isolate the impact of incident irradiation on the evaporation system from that of natural evaporation. However, we posit that this is unnecessary, especially when calculating the evaporation efficiency. Pseudosteady dark environment evaporation is maintained due to environmental energy input, which stems from a negative temperature differential between the evaporation system and the environment. This environmental energy input typically does not manifest during an illuminated solar evaporation test, as this negative temperature differential does not exist. If all regions of the evaporator itself are elevated above the ambient temperature, there will not be energy input from the surroundings. Thus, in a properly isolated evaporation rate test, the evaporator should not receive excess energy from the environment, and there is no need to subtract the evaporation rate from such a source, as noted by Li *et al.* (*12*). Exceptions to this include cases with unique geometries designed to harvest environmental energy input, such as three-dimensional evaporators (*13*, *28*). However, even for these exceptions, the surrounding energy input is highly dependent on ambient conditions (temperature and humidity), which influence input heat transfer and evaporation rate. In an illuminated evaporation rate test, these conditions will certainly be modified, and the input energy cannot be assumed to be the same as that of a dark environment test. While the dark environment rate may be subtracted in these cases for an estimate of the pure, solar-driven evaporation, this method provides, at best, only a conservative estimate (*12*). For these reasons, simply subtracting the dark environment evaporation rate from the solar-driven evaporation rate is inaccurate and unnecessary for the calculation of the solar-to-vapor conversion efficiency in most systems, as the environmental energy input that sustains dark evaporation is not identical (and in most cases does not manifest) in a typical illuminated test.

Last, recent discussions in the literature call into question the current understanding of reduced enthalpy of evaporation during continuous interfacial solar evaporation processes. A modification of the water state clearly manifests in many materials (most notably hydrogels) and may produce a reduced DSC-measured enthalpy value, often accompanied by solar-driven evaporation rates above the theoretical limit (*1*). However, when considering the energy balance of the entire system, the enthalpy of the water before inundation within the hydrogel is unchanged from its theoretical bulk value. Thus, in a continuous system, energy should be consumed to raise the water's enthalpy from the bulk value to the modified value when it is absorbed into the hydrogel. This process must consume energy, as noted by Ducker (*29*). For this reason, it seems impossible that reductions in water vaporization enthalpy would manifest in a continuous evaporation system if the phenomena were based purely on a modification of the bonding state of hydrogel-absorbed water.

Our experimental data lend support to this theory. First, it shows that typical claims of enthalpy reduction in a continuous dark environment evaporation test are likely invalid, offering the alternative explanation of energy input discrepancies. In addition, we illustrate the contradictory nature of continuous (dark environment) and noncontinuous (DSC) enthalpy characterization methods, challenging the supposed relationship between enthalpies characterized using these approaches, as well as the current understanding of vaporization enthalpy reduction as a whole. Rather, alternative theories that involve extra energy input coming from outside of the evaporation system would provide a more reasonable explanation, such as those that posit the breakup of released water clusters outside of the evaporator system (*21*). This would also help explain how evaporation materials besides hydrogels have been reported to break the theoretical limit, even without a modification of the water state.

In summary, a critical assessment of reduced enthalpy characterization through dark environment evaporation testing is performed. The assumption of equal energy input between a water system and an interfacial evaporator system is analyzed both theoretically and experimentally. In both cases, the environmental energy input to the interfacial evaporation system is shown to substantially exceed that of the water system. The excess energy input within the experimental test is calculated using a transient analytical model, and it is found that the enhancement in evaporation for the interfacial evaporator agrees with the enhancement of energy input due to lower evaporator temperatures. These data illustrate that the assumption of equal energy input is not valid and that reduced values of enthalpy obtained using this characterization method are not accurate. Recent uses of the dark environment characterization method in the literature are analyzed with respect to these results, and it is found that the magnitude of previously reported dark environment data matches well with our explanation of excess energy input. Discrepancies with DSC characterizations are also discussed, emphasizing that the current understanding of vaporization enthalpy reduction

in interfacial evaporation systems requires reconsideration. Further efforts by the scientific community are vital to advance our understanding of the complex vaporization phenomena that occur during solar-driven evaporation. A deeper understanding of how the vaporization energy requirement may be effectively reduced, materials that facilitate these phenomena, and suitable characterization methods will provide noteworthy progress toward global sustainability.

## MATERIALS AND METHODS

### Materials

Commercially available MF sponges are obtained from South Street Designs Company (UPC: 089902974060). PVA (CAS 9002-89-5) is obtained from MP Biomedicals. Glutaraldehyde (CAS 111-30-8, 50 wt % in $H_2O$) and hydrochloric acid (HCl 37%, CAS 7647-01-0) are obtained from Sigma-Aldrich. Carbon nanoparticles (CNPs, 100 nm and below) are obtained from US Research Nanomaterials (stock no. US1076).

### Sample preparation

To prepare the MF sponge sample, the sponge is rinsed three times with DI water and ethanol before use. It is cut to a thickness of 10 mm and a 41 mm diameter to fit within the test beaker during evaporation tests.

PVA hydrogels are synthesized based on the procedures of recent representative works in the literature (*3*, *20*, *21*). For PVA-7.5 samples, a modified procedure based on that of Guo *et al.* (*20*) is used. First, 0.75 g of PVA is combined with 10 ml of DI water and 94 μl of glutaraldehyde solution. The mixture is stirred at 30°C under vigorous magnetic stirring for 1 hour to yield a homogeneous solution. Then, the mixture is removed from the heat, and 37.5 mg of CNPs is added to the solution. The mixture is continuously stirred as it comes to room temperature. As needed, the solution is placed in a centrifuge at 2000 rpm for 10 min to remove bubbles. Then, the mixture is placed in an ultrasonicator, and 0.5 ml of 1.2 M HCl solution is added. After ultrasonicating for 2 min, the combined solution is poured into an aluminum petri dish, yielding a thickness of approximately 2 mm. After gelling at room temperature for 90 min, the gel is removed and placed in DI water overnight. Then, soaked samples are frozen on a liquid nitrogen-cooled steel plate. The steel plate is placed in an insulated cooler and doused in liquid nitrogen. Once the nitrogen evaporates fully, the plate temperature is approximately −50°C. The samples, placed within aluminum trays, are frozen for 1 hour on the chilled plate. Additional nitrogen is added as needed to maintain a plate temperature below −30°C. Immediately afterward, the samples are freeze-dried in a Labconco FreeZone freeze dryer for 48 hours at a collector temperature of −105°C. After freeze drying, samples are soaked in DI water at 80°C for 2 hours to remove residual chemicals. Last, samples are fully swelled in fresh DI water for testing and characterization.

For PVA-10 samples, a similar procedure is used, based on those of Tu *et al.* (*21*) and Zhao *et al.* (*3*). First, 1 g of PVA is combined with 10 ml of DI water and 62.5 μl of glutaraldehyde solution. The mixture is stirred at 80°C under vigorous magnetic stirring for 1 hour to yield a homogeneous solution. Then, the mixture is removed from the heat, and 50 mg of CNPs are added to the solution. The mixture is continuously stirred as it comes to room temperature. As needed, the solution is placed in a centrifuge at 2000 rpm for 10 min to remove bubbles. Then, the mixture is placed in an ultrasonicator, and 1 ml of 1.2 M HCl solution is added. After ultrasonicating for 2 min, the combined solution is poured into an aluminum petri dish. After gelling at room temperature for 2 hours, the gel is removed and placed in DI water overnight. Next, soaked samples undergo a freeze-thawing process using a liquid nitrogen–cooled steel plate. The liquid nitrogen freezing process is the same as the PVA-7.5 samples, but is extended for 2 hours. After each freezing process, samples are thawed at room temperature for 30 min, followed by soaking in DI water for 30 min. The freeze-thaw process is repeated 5 times for PVA-10-FTx5 and 1 time for PVA-10-FTx1. After completing the prescribed number of cycles, samples are frozen once using the same liquid nitrogen process for 1 hour. Immediately afterward, the samples are freeze-dried in a Labconco FreeZone freeze dryer for 48 hours at a collector temperature of −105°C. After freeze drying, samples are soaked in DI water at 80°C for 2 hours to remove residual chemicals. Last, samples are fully swelled in fresh DI water for testing and characterization.

### Evaporation tests

Evaporation tests were performed over a test period of 24 hours in a closed darkroom environment. Two polypropylene beakers containing DI water were placed side by side, undisturbed during the entire test period. The MF sponge is placed on the water surface of the evaporator beaker, in direct contact with the DI water. It is pushed into the beaker until its top surface is in line with the mouth of the beaker. The same treatment is used for the PVA hydrogel samples. The beakers were surrounded on the sides by 42 mm of polyvinyl chloride (PVC) insulation foam (measured thermal conductivity of 0.065 W $m^{-1}$ $K^{-1}$). The beakers were placed on top of 38 mm of polystyrene (PS) insulation foam (measured thermal conductivity of 0.047 W $m^{-1}$ $K^{-1}$) and another 12.7 mm of PVC insulation foam. Insulation boards were firmly secured to one another to diminish contact resistance. Temperatures were monitored using the FLIR A655C thermal camera with a resolution of 640 × 480 using a 25° lens. Temperatures for evaporator system surfaces were taken as the average over each respective surface. Transparent acrylic sheets were positioned around the setup to reduce the impact of ambient temperature and wind fluctuations during the test. This enclosure is not air-tight, so that evaporating water vapor will not accumulate locally. Ambient temperature was monitored using a thermocouple positioned inside of the wind-covered area. An additional thermocouple was secured to the inside of one acrylic sheet to monitor the temperature of the walls inside the enclosure. The enclosure wall temperature was used as the surrounding temperature for the radiative transfer calculation. Agreement between thermocouple and IR temperatures within ±0.05°C is confirmed before testing. The mass of each water-filled test beaker (plus evaporator, when applicable) was weighed before and after each test period using the RADWAG PS 1000 electronic scale. Masses were not continuously monitored by the scale to avoid excess heat input from the scale and to allow the two beakers to remain sufficiently close to one another to achieve identical ambient conditions. As the evaporation surface temperature drops very rapidly once the beakers are prepared during setup, the initial temperature of the bulk water used to fill each beaker is measured via a thermocouple before each test, within 5 min of the start time. This temperature is used as the initial domain temperature in the analysis. Humidity was monitored using the WS-2000 weather station with the WH32B sensor, and is reported for each test within the Supplementary Materials.

### Characterization

DSC curves were performed on the TA Instruments Q2000 DSC under Argon flow (50 ml $min^{-1}$) using a scanning rate of 10°C $min^{-1}$ for high-temperature tests and 5°C $min^{-1}$ for low-temperature tests. A rate of 5°C $min^{-1}$ is common throughout the literature to provide good data fidelity; however, it was found that the higher scanning rate yielded a slightly more accurate characterization of the control water vaporization enthalpy and boiling point, as shown in the Supplementary Materials. Sample masses used for DSC characterization are also given in the Supplementary Materials. Thermal conductivity is characterized using the HotDisk TPS 2500s. SEM images were obtained from the Supra 25 SEM using an acceleration voltage of 5 kV. Fourier transform infrared spectroscopy (FTIR) spectra are obtained using the Jasco FTIR 6600 equipped with a 12° incidence PIKE integrating sphere.

## Supplementary Materials

**This PDF file includes:**

Supplementary Text
Figs. S1 to S16
Tables S1 to S4
References

## REFERENCES AND NOTES


1. D. Wei, C. Wang, J. Zhang, H. Zhao, Y. Asakura, M. Eguchi, X. Xu, Y. Yamauchi, Water activation in solar-powered vapor generation. *Adv. Mater.* **35**, 2212100 (2023).
2. P. Tao, G. Ni, C. Song, W. Shang, J. Wu, J. Zhu, G. Chen, T. Deng, Solar-driven interfacial evaporation. *Nat. Energy* **3**, 1031–1041 (2018).
3. F. Zhao, X. Zhou, Y. Shi, X. Qian, M. Alexander, X. Zhao, S. Mendez, R. Yang, L. Qu, G. Yu, Highly efficient solar vapour generation via hierarchically nanostructured gels. *Nat. Nanotechnol.* **13**, 489–495 (2018).
4. X. Zhou, F. Zhao, Y. Guo, B. Rosenberger, G. Yu, Architecting highly hydratable polymer networks to tune the water state for solar water purification. *Sci. Adv.* **5**, eaaw5484 (2019).
5. A. Caratenuto, L. Xie, L. Gu, Y. Tian, X. Liu, C. Wang, M. Su, Y. Zheng, Adobe bricks as zero-material-cost solar evaporators for water-scarce regions. *Desalination* **546**, 116199 (2023).
6. Q.-F. Guan, Z.-M. Han, Z.-C. Ling, H.-B. Yang, S.-H. Yu, Sustainable wood-based hierarchical solar steam generator: A biomimetic design with reduced vaporization enthalpy of water. *Nano Lett.* **20**, 5699–5704 (2020).
7. X. Liu, Y. Tian, F. Chen, R. Ahlgren, Y. Zheng, M. Su, G. Xiao, Y. Zheng, An efficient and scalable strategy for ultrablack-paint-enabled solar-driven steam generation. *Sol. Energy Mater. Sol. Cells* **234**, 111436 (2022).
8. Y. Tian, X. Liu, J. Li, Y. Deng, J. A. De Giorgis, S. Zhou, A. Caratenuto, M. L. Minus, Y. Wan, G. Xiao, Y. Zheng, Farm-waste-derived recyclable photothermal evaporator. *Cell Rep. Phys. Sci.* **2**, 100549 (2021).
9. B. Yang, Z. Zhang, P. Liu, X. Fu, J. Wang, Y. Cao, R. Tang, X. Du, W. Chen, S. Li, H. Yan, Z. Li, X. Zhao, G. Qin, X.-Q. Chen, L. Zuo, Flatband λ-$Ti_3O_5$ towards extraordinary solar steam generation. *Nature* **622**, 499–506 (2023).
10. Z. Li, Y. Zhang, Q. Huang, Z. Chen, W. Wang, W. Li, Tailorable lignocellulose-based aerogel to achieve the balance between evaporation enthalpy and water transport rate for efficient solar evaporation. *ACS Appl. Mater. Interfaces* **15**, 11827–11836 (2023).
11. F. P. Incropera, D. Dewitt, Eds., *Fundamentals of Heat and Mass Transfer* (John Wiley, ed. 6, 2007).
12. X. Li, G. Ni, T. Cooper, N. Xu, J. Li, L. Zhou, X. Hu, B. Zhu, P. Yao, J. Zhu, Measuring conversion efficiency of solar vapor generation. *Joule* **3**, 1798–1803 (2019).
13. X. Liu, Y. Tian, F. Chen, A. Caratenuto, J. A. De Giorgis, M. ELSonbaty, Y. Wan, R. Ahlgren, Y. Zheng, An easy-to-fabricate 2.5D evaporator for efficient solar desalination. *Adv. Funct. Mater.* **31**, 2100911 (2021).
14. M. Bongarala, H. Hu, J. A. Weibel, S. V. Garimella, A figure of merit to characterize the efficacy of evaporation from porous microstructured surfaces. *Int. J. Heat Mass Transf.* **182**, 121964 (2022).
15. Z. Yu, R. Gu, Y. Tian, P. Xie, B. Jin, S. Cheng, Enhanced interfacial solar evaporation through formation of micro-meniscuses and microdroplets to reduce evaporation enthalpy. *Adv. Funct. Mater.* **32**, 2108586 (2022).
16. Y. Feng, J. Yao, Design of melamine sponge-based three-dimensional porous materials toward applications. *Ind. Eng. Chem. Res.* **57**, 7322–7330 (2018).
17. Q. Hou, C. Xue, N. Li, H. Wang, Q. Chang, H. Liu, J. Yang, S. Hu, Self-assembly carbon dots for powerful solar water evaporation. *Carbon* **149**, 556–563 (2019).
18. MathWorks, Partial Differential Equation Toolbox. Mathworks.com/help/pde/.
19. M. Moran, H. Shapiro, D. Boettner, M. Bailey, *Fundamentals of Engineering Thermodynamics* (John Wiley & Sons, ed. 7, 2011).
20. Y. Guo, X. Zhou, F. Zhao, J. Bae, B. Rosenberger, G. Yu, Synergistic energy nanoconfinement and water activation in hydrogels for efficient solar water desalination. *ACS Nano* **13**, 7913–7919 (2019).
21. Y. Tu, J. Zhou, S. Lin, M. Alshrah, X. Zhao, G. Chen, Plausible photomolecular effect leading to water evaporation exceeding the thermal limit. *Proc. Natl. Acad. Sci. U.S.A.* **120**, e2312751120 (2023).
22. H. Adelnia, R. Ensandoost, S. S. Moonshi, J. N. Gavgani, E. I. Vasafi, H. T. Ta, Freeze/thawed polyvinyl alcohol hydrogels: Present, past and future. *Eur. Polym. J.* **164**, 110974 (2022).
23. G. Chen, Thermodynamics of hydrogels for applications in atmospheric water harvesting, evaporation, and desalination. *Phys. Chem. Chem. Phys.* **24**, 12329–12345 (2022).
24. W. Li, F. Xue, R. Cheng, States of water in partially swollen poly(vinyl alcohol) hydrogels. *Polymer* **46**, 12026–12031 (2005).
25. T. Nakaoki, H. Yamashita, Bound states of water in poly(vinyl alcohol) hydrogel prepared by repeated freezing and melting method. *J. Mol. Struct.* **875**, 282–287 (2008).
26. J. M. Serrano, T. Liu, D. Guo, Z. L. Croft, K. Cao, A. U. Khan, Z. Xu, E. Nouh, S. Cheng, G. Liu, Utilization of block copolymers to understand water vaporization enthalpy reduction in uniform pores. *Macromolecules* **55**, 4803–4811 (2022).
27. X. Luo, J. Shi, C. Zhao, Z. Luo, X. Gu, H. Bao, The energy efficiency of interfacial solar desalination. *Appl. Energy* **302**, 117581 (2021).
28. J. Tang, T. Zheng, Z. Song, Y. Shao, N. Li, K. Jia, Y. Tian, Q. Song, H. Liu, G. Xue, Realization of low latent heat of a solar evaporator via regulating the water state in wood channels. *ACS Appl. Mater. Interfaces* **12**, 18504–18511 (2020).
29. W. A. Ducker, Decreasing the energy of evaporation using interfacial water: Is this useful for solar evaporation efficiency? *ACS Omega* **8**, 19705–19707 (2023).
30. Z. Xu, L. Zhang, L. Zhao, B. Li, B. Bhatia, C. Wang, K. L. Wilke, Y. Song, O. Labban, J. H. Lienhard, R. Wang, E. N. Wang, Ultrahigh-efficiency desalination via a thermally-localized multistage solar still. *Energ. Environ. Sci.* **13**, 830–839 (2020).


**Acknowledgments:** We thank R. Erb, D. Braconnier, and A. Hametz-Berner for facilitating the DSC measurements, as well as H. Ghandour for assistance with hydrogel synthesis. **Funding:** This project is supported by the National Science Foundation through grant number CBET-1941743. **Author contributions:** Conceptualization: A.C. and Y.Z. Methodology: A.C. Validation: A.C. Formal analysis: A.C. Investigation: A.C. Resources: Y.Z. Writing—original draft: A.C. Writing—review and editing: Y.Z. Visualization: A.C. Supervision: Y.Z. Project administration: Y.Z. Funding acquisition: Y.Z. **Competing interests:** The authors declare that they have no competing interests. **Data and materials availability:** All data needed to evaluate the conclusions in the paper are present in the paper and/or the Supplementary Materials.

Submitted 9 March 2024
Accepted 12 August 2024
Published 18 September 2024
10.1126/sciadv.adn6368